

AD \_\_\_\_\_

Award Number: W81XWH-11-1-0229

TITLE: Dynamic Contrast-Enhanced Digital Breast Tomosynthesis

PRINCIPAL INVESTIGATOR: Andrew D. A. Maidment, Ph.D.

CONTRACTING ORGANIZATION: University of Pennsylvania  
Philadelphia, Pennsylvania 19104

REPORT DATE: Ráã'å 2013

TYPE OF REPORT: Final

PREPARED FOR: U.S. Army Medical Research and Materiel Command  
Fort Detrick, Maryland 21702-5012

DISTRIBUTION STATEMENT: Approved for public release;  
distribution unlimited

The views, opinions and/or findings contained in this report are those of the author(s) and should not be construed as an official Department of the Army position, policy or decision unless so designated by other documentation.

| REPORT DOCUMENTATION PAGE   |                              |  | Form Approved<br>OMB No. 074-0188                                |   |
|---|------------------------------|--|--|---|
| Public reporting burden for this collection of information is estimated to average 1 hour per response, including the time for reviewing instructions, searching existing data sources, gathering and maintaining the data needed, and completing and reviewing this collection of information. Send comments regarding this burden estimate or any other aspect of this collection of information, including suggestions for reducing this burden to Washington Headquarters Services, Directorate for Information Operations and Reports, 1215 Jefferson Davis Highway, Suite 1204, Arlington, VA 22202-4302, and to the Office of Management and Budget, Paperwork Reduction Project (0704-0188), Washington, DC 20503   |                              |  |  |   |
| 1. Agency Use Only (Leave blank)  | 2. Report Date<br>Ráã'å 2013 | 3. Report Type and Period Covered (i.e., annual 1 Jun 00 - 31 May 01)<br>Final (1 Ráã'å 20FF - GÏ Ôæãã áã] 2013) |  |   |
| 4. Title and Subtitle<br>Dynamic Contrast-Enhanced Digital Breast Tomosynthesis   |                              | 5. Award Number<br>W81XWH-11-1-0229  |  |   |
| 6. Author(s)<br>Andrew D. A. Maidment, Ph.D.<br>Ó↑ÍÁÁN^ääæ}ÈRá↔ä↑æ^\M *âbÈ *æ^Èæä Á   |                              |  |  |   |
| 7. Performing Organization Name (Include Name, City, State, Zip Code and Email for Principal Investigator)<br>University of Pennsylvania<br>Philadelphia, PA 19104  |                              | 8. Performing Organization Report Number (Leave Blank)   |  |   |
| 9. Sponsoring/Monitoring Agency Name and Address<br>U.S. Army Medical Research and Materiel Command<br>Fort Detrick, Maryland 21702-5012  |                              | 10. Sponsoring/Monitoring Agency Report Number (Leave Blank)   |  |   |
| 11. Supplementary Notes (i.e., report contains color photos, report contains appendix in non-print form, etc.)  |                              |  |  |   |
| 12a. Distribution/Availability Statement (check one)<br>Approved for public release; distribution unlimited   |                              |  | 12b. Distribution Code<br>(Leave Blank)                          |   |
| <b>13. Abstract (Maximum 200 Words) (abstract should contain no proprietary or confidential information)</b><br>Contrast-enhanced digital breast tomosynthesis (CE-DBT) is a novel x-ray imaging technique that produces a 3D representation of the breast vasculature via an intravenous contrast agent. CE-DBT offers a combination of excellent spatial resolution and accurate functional information, suggesting a strong potential role in disease prognostication. We have developed an innovative technique for obtaining dynamic contrast-enhanced (DCE) images with high spatial and temporal resolution. We have demonstrated, in proof-of-principle, that 4D DCE-DBT is technically feasible and that the derived data accurately measures vascular dynamics. Previous contrast-enhanced DBT systems produced images at 2-3 fixed time points. Our novel acquisition technique is capable of producing perfusion images at 30-60 time points for the same radiation dose. The method is compatible with both temporal and dual-energy subtraction methods. Reconstruction is performed using one full set of sequentially-acquired images; however, unlike conventional DBT, the starting angle (and hence measurement time point) is arbitrary in our method. The resulting 4D data set consists of many time-resolved 3D functional measurements of tumor perfusion, offering the potential for superior lesion characterization and hence diagnostic accuracy. |                              |  |  |   |
| 14. Subject Terms (keywords previously assigned to proposal abstract or terms which apply to this award)<br>Breast Cancer, contrast-enhanced imaging, digital breast tomosynthesis, dynamic imaging, x-ray imaging  |                              |  | 15. Number of Pages (count all pages including appendices)<br>55 |   |
| 17. Security Classification of Report<br>Unclassified   |                              |  | 16. Price Code   |   |
| 18. Security Classification of this Page<br>Unclassified  |                              | 19. Security Classification of Abstract<br>Unclassified  |  | 20. Limitation of Abstract<br>Unlimited |

## Table of Contents

|   | <u>Page</u> |
|---|-------------|
| 1. Introduction                               | 5           |
| 2. Keywords                                   | 5           |
| 3. Overall Project Summary                    | 6           |
| 4. Key Research Accomplishments               | 13          |
| 5. Conclusion                                 | 13          |
| 6. Publications, Abstracts, and Presentations | 14          |
| 7. Inventions, Patents and Licenses           | 14          |
| 8. Reportable Outcomes                        | 14          |
| 9. Other Achievements                         | 14          |
| 10. References                                | 15          |
| 11. Appendices                                | 16          |

## FOREWORD

Opinions, interpretations, conclusions and recommendations are those of the author and are not necessarily endorsed by the U.S. Army.

N/A Where copyrighted material is quoted, permission has been obtained to use such material.

N/A Where material from documents designated for limited distribution is quoted, permission has been obtained to use the material.

N/A Citations of commercial organizations and trade names in this report do not constitute an official Department of Army endorsement or approval of the products or services of these organizations.

N/A In conducting research using animals, the investigator(s) adhered to the "Guide for the Care and Use of Laboratory Animals," prepared by the Committee on Care and use of Laboratory Animals of the Institute of Laboratory Resources, national Research Council (NIH Publication No. 86-23, Revised 1985).

X For the protection of human subjects, the investigator(s) adhered to policies of applicable Federal Law 45 CFR 46.

N/A In conducting research utilizing recombinant DNA technology, the investigator(s) adhered to current guidelines promulgated by the National Institutes of Health.

N/A In the conduct of research utilizing recombinant DNA, the investigator(s) adhered to the NIH Guidelines for Research Involving Recombinant DNA Molecules.

N/A In the conduct of research involving hazardous organisms, the investigator(s) adhered to the CDC-NIH Guide for Biosafety in Microbiological and Biomedical Laboratories.



PI - Signature

9/04/13  
Date

## 1) INTRODUCTION:

We have developed a new technique for obtaining 4D dynamic contrast-enhanced (DCE) digital breast tomosynthesis (DBT) images that will allow the measurement of tumor perfusion with improved accuracy. Current contrast-enhanced DBT systems produce images at 2-3 fixed time points. Our novel acquisition technique is capable of producing perfusion images at 30-60 time points for the same radiation dose. The method is compatible with both temporal and dual-energy (DE) subtraction methods. In our new method, a single projection image is acquired, for example, once every 5 seconds. One complete tomosynthesis projection series consists of a set of projection images acquired at distinct angles. In the new method, several complete tomosynthesis projection series are acquired sequentially. Reconstruction is performed using one full set of sequentially-acquired images (or a sufficient subset); however, unlike conventional DBT, the starting angle (and hence measurement time point) is arbitrary in the new method. The resulting 4D data set consists of many time-resolved 3D functional measurements of tumor perfusion, offering the potential for superior lesion characterization and hence diagnostic accuracy. In this grant, we have built and tested the system, including extensive characterizations of spatial resolution and temporal resolution.

- 2) **KEYWORDS:** Contrast-enhanced imaging, x-ray imaging, digital breast tomosynthesis (DBT), 4D imaging, modulation transfer function (MTF), spatial resolution, temporal resolution, contrast agent quantification.

### 3) OVERALL PROJECT SUMMARY:

In this final report, we can demonstrate excellent progress on this project. We presented some aspects of this research<sup>1</sup> at the RSNA Annual Meeting in Chicago in November 2011, and will present our completed results at the RSNA Annual Meeting in Chicago in November 2013. In addition, we have one manuscript submitted and another in preparation.

The primary purpose of this grant is to demonstrate that dynamic 4D DCE-DBT is technologically feasible and results in superior measurements of tumor perfusion. Two objectives were proposed: (#1) Build a DBT prototype to demonstrate, in proof-of-principle, that 4D DCE-DBT is technically feasible. (#2) Develop techniques to derive accurate measures of breast tumor perfusion dynamics. We have successfully completed both aims and are currently in the process of preparing a follow-up grant application to bring this research to the next logical stage – the development of a clinical prototype. We are also in the process of preparing a patent disclosure.

#### Aim 1: System Design and Fabrication

A conceptual diagram of the imaging method is shown in Figure 1. Rather than making three rapid acquisitions of 13 projections each, thereby giving three discrete time points for which to perform contrast-enhanced imaging, we acquire the same number of images (and thus use the same dose); however, each projection image is delayed from the next by a finite period of time. For example, in the example shown, a delay of 5 seconds between each projection image would result in a total acquisition time of 190 sec [ $5 \text{ sec} * (3*13 - 1)$ ]. Reconstructions would then be made at 27 discrete time points [ $2*13 + 1$ ]. In this aim, we proposed to build a proof-of-principle prototype for both the acquisition and reconstruction systems.

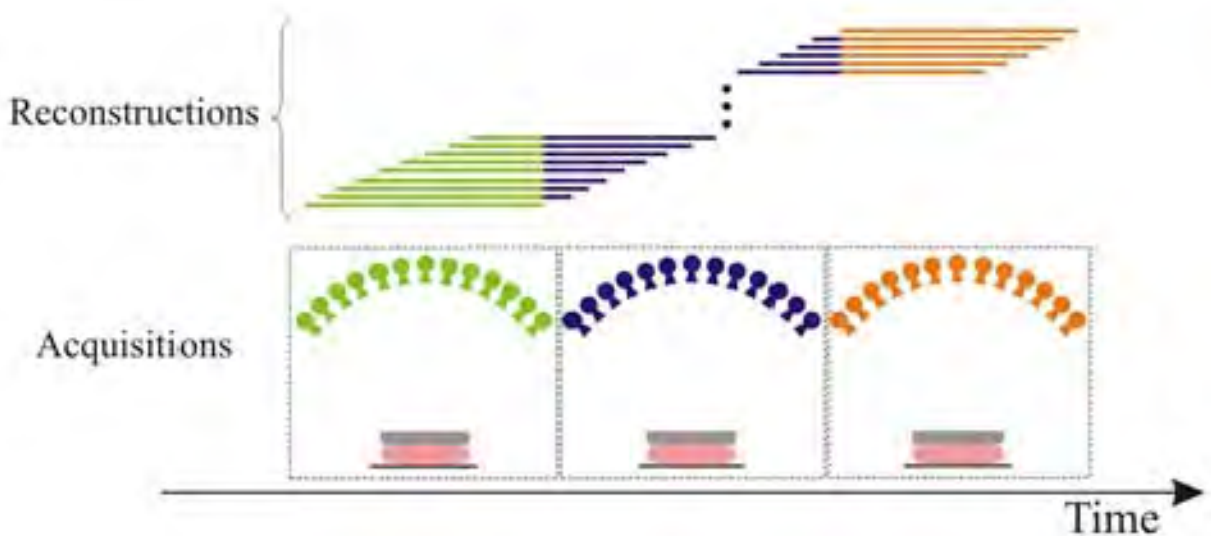


**Figure 1:** Illustration of the acquisition and reconstruction method

We have completed both the design and the fabrication of the imaging system. Projection images are acquired using a custom x ray imaging testing station with x ray source, detector,

rotary stage, and filter as shown in Figure 2. The testing station uses a GE Senographe 500 x ray generator (General Electric Health Care, Chalfont-St. Giles, UK) with a selenium flat-panel detector (Direct Radiography Corp, Newark, DE). Parker Motion stepper motors (Parker Hannifin, Rohnert Park, CA) are used to drive a rotary stage on which a phantom can be mounted and rotated, as well as a custom filter wheel; magnetic sensors are used to precisely control the position of the rotary stage and filter wheel. The filter wheel is laser-cut acrylic with various mounted filter metals, including 0.5 mm of aluminum used in this experiment. Additionally, the x ray tube has a 25  $\mu\text{m}$  molybdenum filter mounted to the exit port.

In a real clinical system, the detector and x-ray tube would move while the patient is held stationary. The system we built rotates the test object, this approach was chosen, as it is easier to make while remaining mathematically equivalent to the clinical approach.

We have also developed a method of preprocessing an existing reconstruction system (Piccolo, Real-time Tomography, LLC) available in our lab to enable reconstruction of the resultant images.

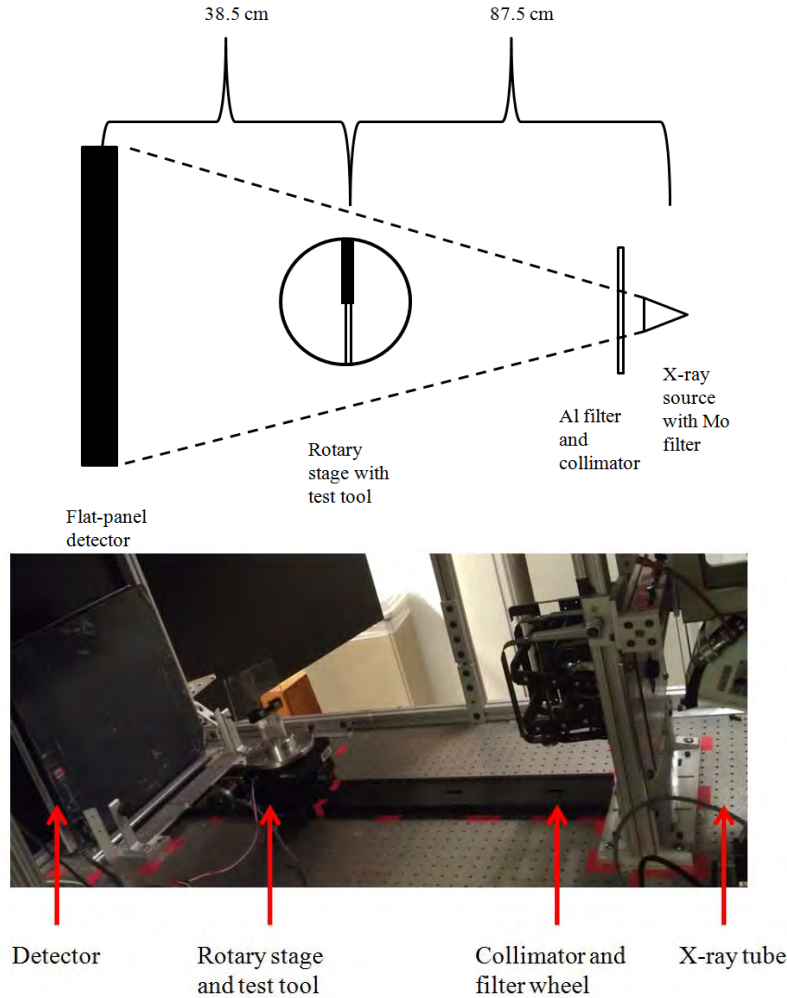


**Figure 2:** (top) The upper image depicts a schematic of custom x-ray imaging station from aerial view. An x-ray source, aluminum filter, and rotary stage with test object are positioned in succession in front of a flat panel detector. (bottom) The image below is a photograph of the x-ray testing station (filter wheel is not visible).

## Aim 2: Quantitation of Iodine Uptake

We have developed a hybrid image subtraction method in which we perform temporal subtraction of the dual-energy images. This technique has several advantages, including the ability to suppress scatter and other artifacts in the dual energy images, insensitivity to motion artifacts, the ability to quantify contrast agent uptake, and good noise performance.

The ability to quantify the iodine in terms of areal density is particularly important. The data, shown in Figure 3, illustrate this principle. Shown in Figure 4a is the subtracted signal as a function of the areal density of the contrast material in a static phantom already in use in the lab<sup>2</sup>. The measurements are breast thickness dependent. Shown are the results for breasts 2 cm and 9 cm thick. The data for multiple thicknesses have been summarized in Fig 4b. These data allowed us to quantify the uptake of tumors in absolute numbers for the first time. These results were presented at the 2011 Annual Meeting of the RSNA<sup>1</sup>.

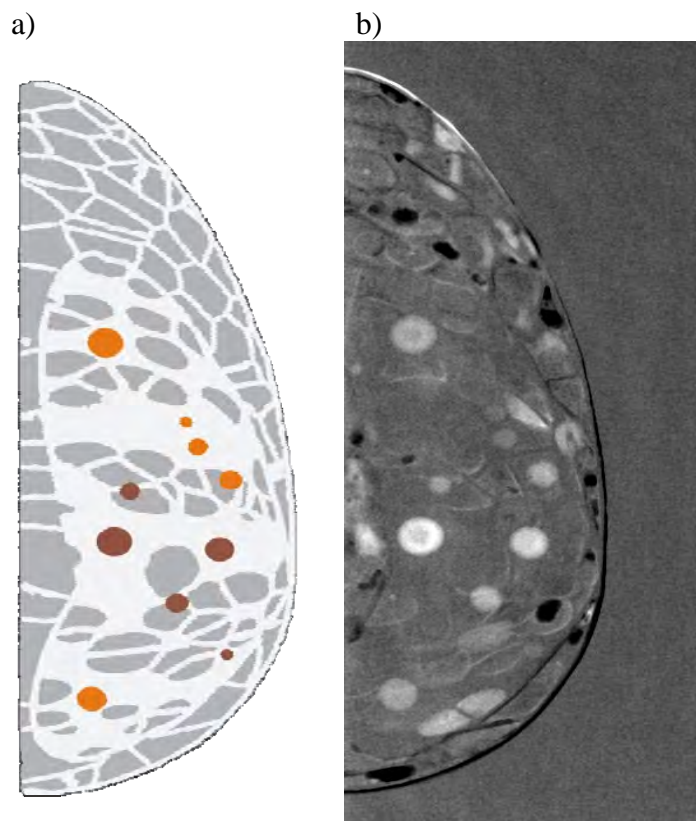


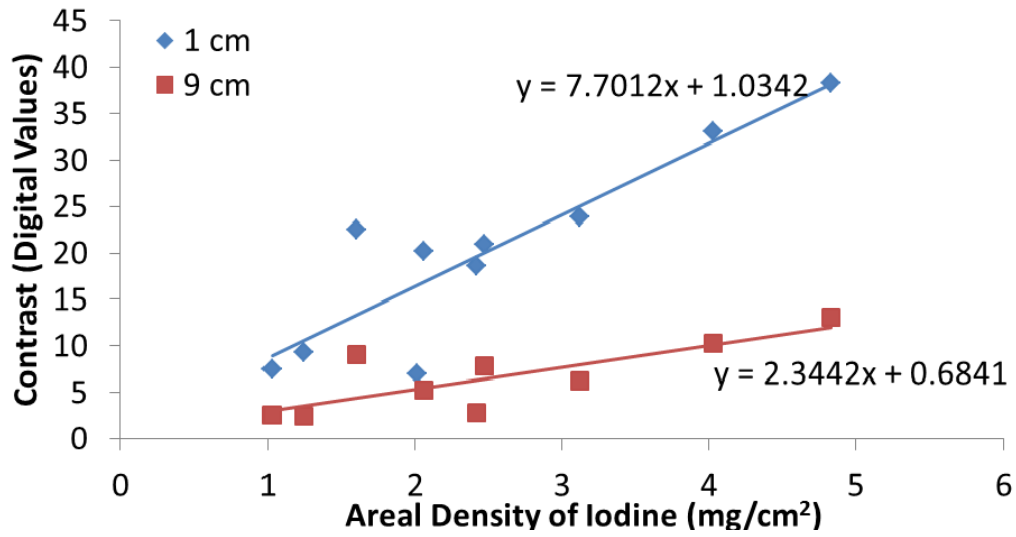
**Figure 3.** (a) A schematic diagram showing one layer of the contrast phantom. The inclusions are specified in Table 1. (b) A hybrid temporal dual-energy subtraction radiograph of the phantom showing the iodine inclusions.



**Table 1:** The phantom illustrated in Figure 2 has 10 iodinated inclusions with the specified size and areal density.

| Lesion depth<br>[mm] | Lesion width<br>[mm] | Areal density [mg I/cm <sup>2</sup> ] |               |
|----------------------|----------------------|---------------------------------------|---------------|
|                      |                      | 5.035 mg I/ml                         | 2.575 mg I/ml |
| 9.6                  | 10.6                 | 4.83                                  | 2.47          |
| 8                    | 8.8                  | 4.03                                  | 2.06          |
| 6.2                  | 7.0                  | 3.12                                  | 1.60          |
| 4.8                  | 5.4                  | 2.42                                  | 1.24          |
| 4                    | 4.6                  | 2.01                                  | 1.03          |

a)



b)

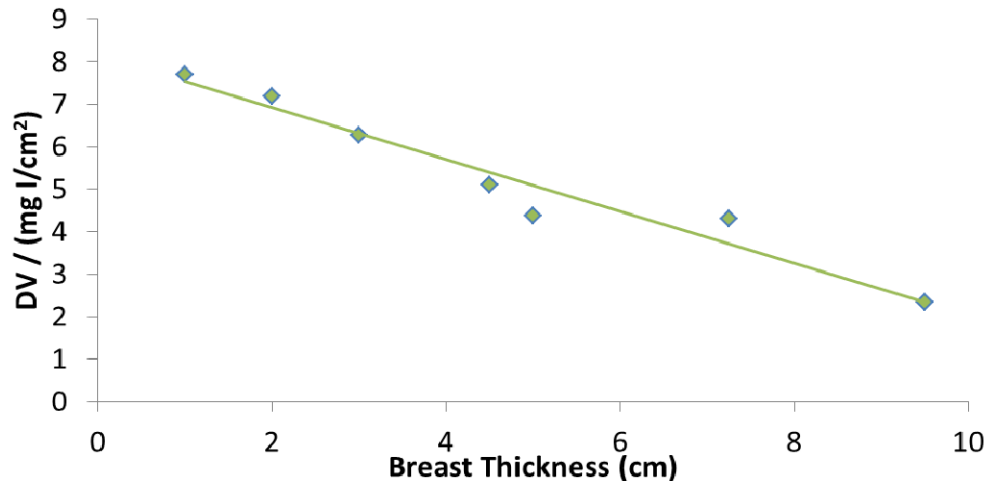


**Figure 4.** (a) Using static phantoms of different thickness, it is possible to quantify the signal as a function of areal density. Two thicknesses are shown for illustration. (b) The calibration coefficient (slope of lines in Fig 4a) can then be calculated for each breast thickness.

It was necessary to estimate the uptake accurately as a function of time, allowing for the fact that the uptake is time varying. Through experimentation, we have found that the uptake is given by the temporal average of the uptake over the time interval used in the reconstruction of the image. In the current reconstruction scheme, the individual source projection images are equally weighted in the reconstruction and the reconstruction (over the key steps) is linear. As such, a moving average is sufficient to model the temporal properties of the imaging system.

These properties were tested with the phantom shown in Figure 5. The concentration of iodine in the circulating fluid was controlled by the addition of contrast agent or distilled water to the circulating fluid. Calibration standards with various concentrations of iodine are included in the phantom to act as a test standard.

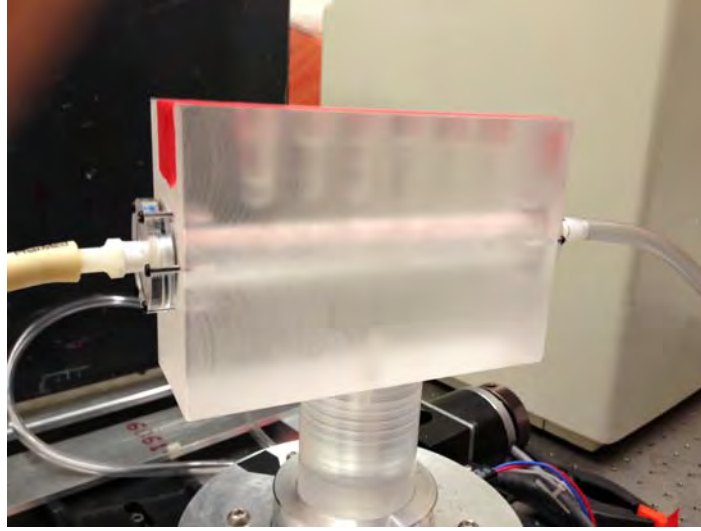


**Figure 5:** A flow phantom was built to simulate temporal dependencies of blood flow in the breast. The phantom consists of a main flow chamber connected to a pump and liquid reservoir. Contrast agent can be added to the reservoir via a power injector (not shown). Six calibration chambers are aligned along the top edge of the phantom.

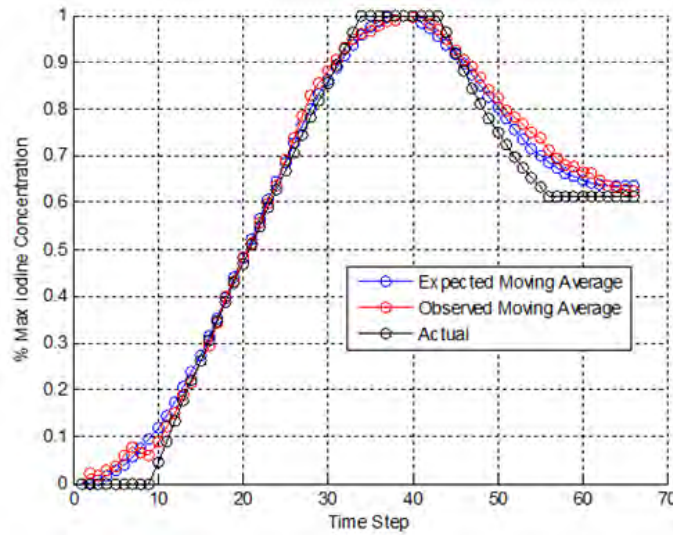


**Figure 6:** A sample temporal measurement of blood flow conducted with the imaging system. The actual iodine concentration is shown (black), together with the expected value (blue) calculated as the moving average of the actual data, and the measured results (red). Close agreement between expected and observed results is seen.

Figure 6 shows the results of one such temporal concentration measurement. The black curve is the actual concentration as determined by the addition of contrast agent and/or distilled water to the circulating fluid. The blue curve is the expected concentration assuming a moving average over the 17 images used in the reconstruction. The red curve is the measured concentration as a function of time. It can be seen from comparison that the theoretical and experimental data match closely.

During the above experiments, it became clear that it was possible to reconstruct tomographic data from a subset of angular measurements; for example, in the examples above, the full data acquisition consisted of reconstructions from projection images measured at 17 unique angles. However, it is possible to perform the reconstruction with any number of unique angles (e.g. 9 angles). In so doing, one is reducing the range of angles used (which reduces z-resolution), and the center angle will vary with time.

The most significant effort was with regard to the spatial resolution. Given that this problem has similar origins to the problem of oblique reconstructions in tomosynthesis<sup>3,4</sup> (for which we have recently had two papers accepted to Medical Physics), we spent considerable time and effort to understand the implications of these changes.

The details of these results are provided in the attached manuscript. Provided here is a brief summary of the results seen in Figure 7. The MTF is computed using the algorithm described by Carton *et al*<sup>5,6</sup>. For the tomosynthesis reconstructions, the MTF is computed by taking the MTF of an edge in a slice of the reconstruction. Briefly, the procedure is as follows:

1. A rectangular region of interest (of 750 x 350 pixels or 80.3 x 37.5 mm) including the edge is selected.
2. A derivative filter is used to find the edge.
3. The edge is interpolated and a super-sampled edge spread function (ESF) is computed over the ROI using a sliding window with a sub-region column size of 20.
4. A monotonic filter is used to reduce the noise of the ESF<sup>7</sup>.
5. The line spread function (LSF) is computed by differentiation of the ESF with a differentiation kernel of [-1 1] and correction for finite element differentiation.
6. The MTF is computed by taking the Fourier transform of the LSF.

The effect of the reconstruction slice offset relative to the plane that contains the edge was measured by obtaining reconstruction slices in 0.1 mm increments from the true slice depth containing the edge. This was performed to estimate the slice spacing that is necessary to produce a reconstruction data set that is minimally degraded with respect to the spatial resolution. These data are summarized in Figure 7B and 7C. It was found that the optimal slice spacing is dependent upon the acquisition geometry.

The effect of the reconstruction slice angle in an oblique reconstruction on the MTF was assessed by changing the angle of the lead sheet with respect to the detector in the reconstruction. These data are summarized in Figure 7D. They show that there is only a small reduction in spatial resolution as the angle of the reconstructed plane is varied (e.g., in oblique reconstructions).

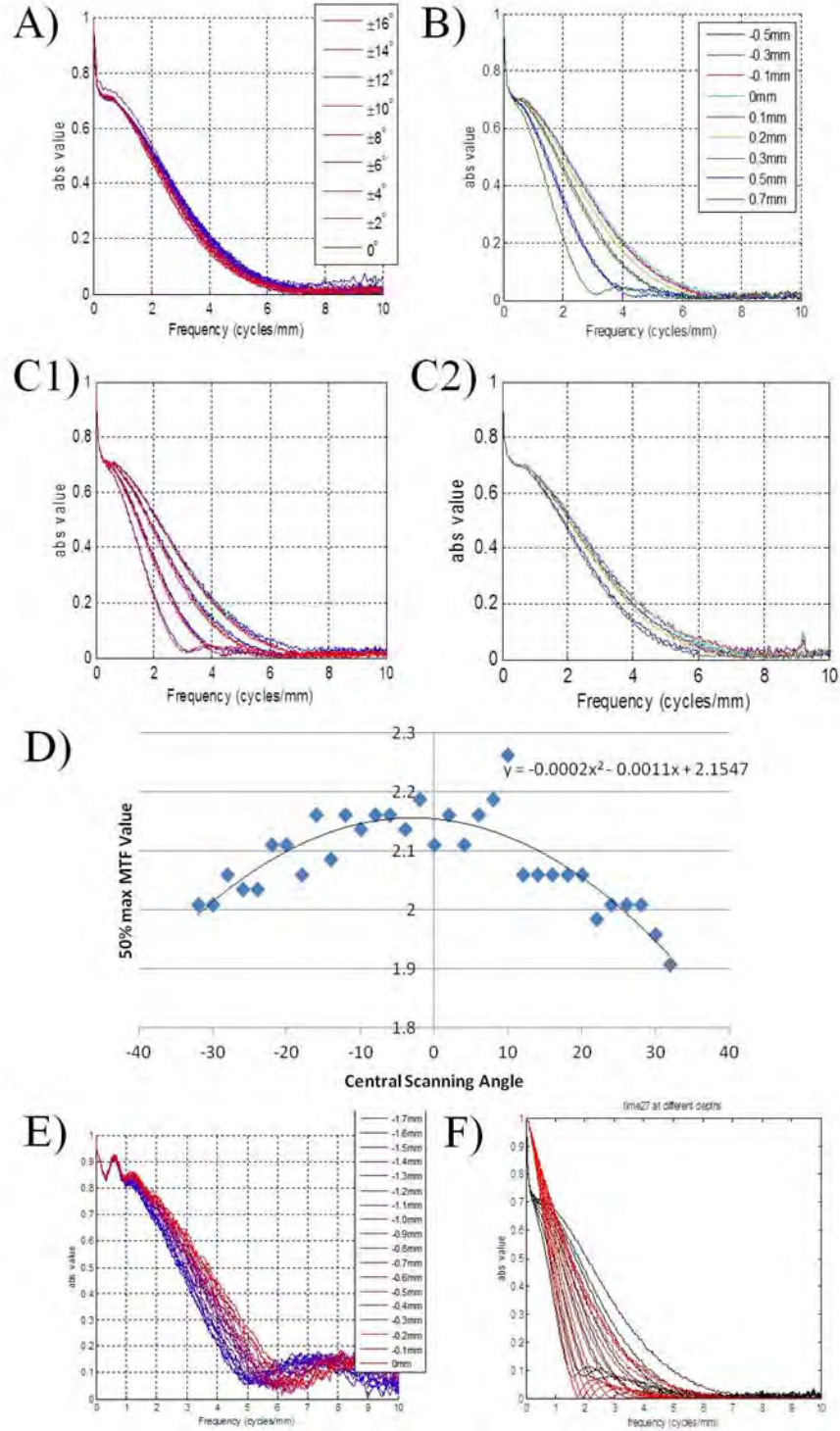


**Figure 7:** Various characterizations of the spatial resolution of the imaging system. A) the dependency of the MTF on the acquisition angular range; B) the dependency of the resolution on the plane of focus of the reconstruction relative to the position of the edge phantom; C) the MTF of the system with (1) 32° angular range, 17 projections (blue) and 9 projections (red), and (2) 32° angular range, 17 projections (blue) and 9 projections (red); D) Reduction in MTF as a function of the central scanning angle; E) Confirmation of MTF results using a clinical tomosynthesis system; F) Simulated (red) vs actual (black) MTF data.

The effect of the number of projections used to create a reconstruction on the MTF was assessed by reducing the number of projections to a subset of the 17 acquired projections. These data are shown in Figure 7A, and 7C. When the number of projections is changed (but the total angle spanned is held constant) there is little effect on spatial resolution. As the number of projections and total angle spanned is changed together, there is a significant reduction improvement in resolution.

Separate validation of these data was performed on a clinical tomosynthesis system (Figure 7E), and a simulation of the spatial resolution was generated. This simulation shows good agreement with experimental results.

The paper on spatial resolution (See Appendix) is currently under review. The paper on the design of the system and the temporal resolution is currently being written.

#### **4) KEY RESEARCH ACCOMPLISHMENTS:**

- Designed prototype dynamic contrast enhanced imaging system intended for proof-of-principle experiments.
- Fabricated and assembled the components, including main gantry, filter wheel, collimator, phantom holder and detector assembly.
- Fabricated x-ray generator interface, including dual-energy control
- Wrote all image acquisition software, including integration of the x-ray generator, motor controllers and x-ray detector software
- Developed a method for quantitative reconstruction of contrast-enhanced images with scatter and thickness suppression.
- Designed a number of key phantoms
- Performed experiments in quantifying the contrast agent uptake.
- Performed experiments determining the temporal characteristics of the system
- Performed experiments determining the spatial characteristics of the system
- Demonstrated that 4D time-resolved contrast-enhanced DBT is feasible
- Working to report these results
- Working to write next grant to continue this research.

#### **5) CONCLUSIONS:**

We have successfully demonstrated in proof-of-principle that 4D DCE-DBT can be achieved in a dose-neutral fashion. The temporal and spatial resolution properties are well understood. These results will allow us to write and submit the next phase of this research – the construction of a clinical system for clinical trial. In addition, we have begun to write up these results for publication in the peer-reviewed literature, and we will seek patent protection for the acquisition, reconstruction and image processing methods.

## 6) PUBLICATIONS, ABSTRACTS, AND PRESENTATIONS:

**Brian C. Lee, Raymond J. Acciavatti, Ph.D., Andrew. D. A. Maidment, Ph.D.** *Dependence of the in-plane Modulation Transfer Function on Acquisition Geometry and Reconstruction Parameters in Tomosynthesis.* Submitted to Medical Physics for peer-review, June 2013

**Brian C. Lee BS, Susan Ng MS, Johnny Kuo, PhD, Peter A. Ringer, BS, Andrew D. A. Maidment PhD.** *Dynamic four-dimensional dynamic contrast-enhanced tomosynthesis.* Accepted for presentation at the RSNA 2013, Chicago IL, November 2013

**Brian C. Lee BS, Andrew D. A. Maidment PhD.** *Characterization of the dependence of the modulation transfer function in tomosynthesis on acquisition geometry and reconstruction parameters.* Accepted for presentation at the RSNA 2013, Chicago IL, November 2013

## 7) INVENTIONS, PATENTS AND LICENSES:

Patent disclosure in preparation.

## 8) REPORTABLE OUTCOMES: N/A

## 9) OTHER ACHIEVEMENTS:

Brian C Lee, MSc, Bioengineering, University of Pennsylvania, May 2103

## 10) REFERENCES:

1. Karunamuni R, Gavenonis SC, Ren B, Ruth C, Maidment ADA. Technical Characterization of a Contrast-enhanced Digital Breast Tomosynthesis System. RSNA 97th Scientific Assembly and Annual Meeting November 2011; Chicago, IL, p., 2011.
2. Carton AK, Bakic P, Ullberg C, Derand H, Maidment AD. Development of a physical 3D anthropomorphic breast phantom. Med Phys. 2011 Feb;38(2):891-6.
3. Acciavatti R, Maidment ADA. Experimental and Theoretical Validation of Breast Tomosynthesis along Oblique Planes. Med Phys. 2011;38(6).
4. Acciavatti RJ, Mein SB, Maidment ADA, editors. Investigating Oblique Reconstructions with Super-Resolution in Digital Breast Tomosynthesis. Breast Imaging; 2012; Philadelphia, PA. 7361 2012.
5. Carton AK, Vandenbroucke D, Struye L, Maidment AD, Kao YH, Albert M, et al. Validation of MTF measurement for digital mammography quality control. Medical Physics. 2005;32(6):1684-95.
6. Kao Y-H, Maidment ADA, Albert M, Carton A-K, Bosmans H, editors. Assessment of a software tool for measurement of the modulation transfer function. Medical Imaging 2005: Physics of Medical Imaging; 2005; San Diego. SPIE. 5745.
7. Maidment ADA, Albert M. Conditioning data for calculation of the modulation transfer function. Medical Physics. 2003;30(2):248-53.

## 11) APPENDICES:

**Brian C. Lee, Raymond J. Acciavatti, Ph.D., Andrew. D. A. Maidment, Ph.D.** *Dependence of the in-plane Modulation Transfer Function on Acquisition Geometry and Reconstruction Parameters in Tomosynthesis.* Submitted to Medical Physics for peer-review, June 2013



# **Dependence of the in-plane Modulation Transfer Function on Acquisition Geometry and Reconstruction Parameters in Tomosynthesis**

Brian C. Lee, Raymond J. Acciavatti, Ph.D., Andrew. D. A. Maidment, Ph.D.

5

*Department of Radiology  
Perelman School of Medicine at the University of Pennsylvania  
Philadelphia, Pennsylvania*

10

15

Abbreviated Title: Characterization of MTF in Tomosynthesis

20

Contact Information:

Andrew D. A. Maidment, Ph.D. FAAPM

Perelman School of Medicine at the University of Pennsylvania

Department of Radiology – Physics Section

25

1 Silverstein Building

3400 Spruce Street

Philadelphia, PA 19104-4206, USA

30

Voice: 215-746-8763

Fax: 215-746-8764

Email: [Andrew.Maidment@uphs.upenn.edu](mailto:Andrew.Maidment@uphs.upenn.edu)

## **ABSTRACT**

### **PURPOSE**

35 The purpose of this work is to characterize the spatial dependence of the in-plane modulation transfer function (MTF) in tomosynthesis and investigate the influence of the acquisition geometry.

### **METHODS**

40 The in-plane MTF was calculated from measured edge spread functions using a custom test tool consisting of a 0.250 mm thick lead sheet affixed to a 5.88 mm acrylic sheet. Images were obtained using a non-clinical bench-top tomosynthesis system; reconstructions were performed using customized commercial software. The dependence of the MTF was measured with respect to the following factors: 1) the offset of the  
45 reconstruction plane from the plane containing the edge; 2) the obliquity of the reconstruction plane with respect to the detector; 3) the number of projections per reconstruction; and 4) the acquisition's angular range. Findings were validated by developing an analytical model of the MTF (accounting for blurring due to focal spot size, magnification, reconstruction pixel size, out-of-focus plane, and reconstruction  
50 blurring) and by replicating the experiment on a clinical tomosynthesis system.

### **RESULTS**

The MTF is degraded when the edge is located between two reconstruction planes. The degree of degradation of the MTF increases as the distance between the edge and the  
55 reconstruction plane increases and as the angular range of acquisition increases. Degradation increases very slightly as the obliquity of the reconstruction plane with respect to the detector increases over the range 0° to 32°. The number of projections per reconstruction does not affect the degradation. The simulated MTFs generated by the analytical model were concordant with findings of the MTF degradation factors, and a  
60 validation experiment on a clinical tomosynthesis system provided independent confirmation that the MTF degrades with increasing distance between the edge and the reconstruction plane.

### **CONCLUSION**

65 The MTF of tomosynthesis systems is spatially anisotropic and varies with sub-slice spacing. Reconstruction of oblique planes results in minimal degradation of the MTF and thus may be clinically acceptable.

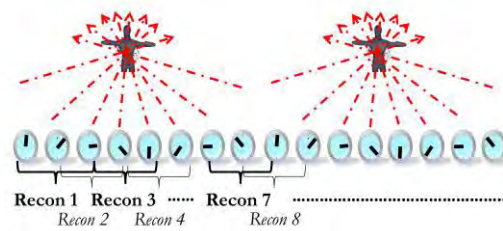
70 Key words: Digital breast tomosynthesis (DBT), 4D imaging, modulation transfer function (MTF), spatial resolution.

## I. INTRODUCTION

Digital breast tomosynthesis has become widely adopted in breast cancer screening by alleviating the obscuration of overlapping breast features. Although tomosynthesis provides accurate three-dimensional localization and visualization of features, its effectiveness is still limited in the detection of tumors that do not demonstrate readily discernible mammographic features<sup>1</sup>. Breast magnetic resonance (MR) imaging is sensitive to such tumors because abnormal metabolic activity associated with tumor growth can be visualized using vascular contrast agents, but MR lacks the ability to visualize microcalcifications and other subtle signs of many breast cancers<sup>2-4</sup>.

By combining the merits of these methods, four-dimensional dynamic contrast-enhanced (4D-DCE) tomosynthesis may be able to improve the accuracy and precision of breast cancer screening. 4D-DCE tomosynthesis involves the injection of a radio-opaque contrast agent through the tissue of interest, and acquiring sets of projections (each of which produces a 3D reconstruction) at different time-points as the contrast agent moves through the tissue. The movement of the contrast agent through the tissue should be observable from analysis of the 3D volume created at each time-point. Thus, 4D-DCE imaging would allow the 3D visualization of blood flow in the breast over time; perfusion data can help draw conclusions about abnormal angiogenesis, which is a well-characterized precursor to tumor development<sup>5</sup>. At the same time, the tomosynthesis data can provide accurate anatomical information.

Obtaining time-resolved reconstructions by current tomosynthesis techniques would require the acquisition of multiple series of tomosynthesis data over a number of time-points, with each reconstruction produced by a full set of projections from each time-  
 95 point. This method would greatly increase the radiation dose to the patient. To address this issue, we have investigated a method to generate four-dimensional reconstructions from a limited set of projections in which only one projection is acquired per time-point and each sequential projection is acquired at a different angle. We hypothesize that accurate time-series data could be produced by reconstructing limited subsets of these  
 100 projections (e.g. applying a sliding window over the set of projections), and even using subsets that do not span the entire angular range of acquisition. Figure 1 shows a schematic representation of a hypothetical reconstruction scheme in which projections at eight angles are acquired at different times, and subsets of three projections are used for reconstruction.



105

**Figure 1:** A hypothetical reconstruction scheme in which projections at eight different angles are acquired at different time-points and two sweeps are made across these eight angles. Three projections are used per reconstruction.

110 In order to identify the lower limit of resolvable features of reconstructions produced by  
such a 4D-DCE tomosynthesis system, we have sought to characterize the spatial  
dependence of the in-plane modulation transfer function (MTF) in tomosynthesis and  
investigate the influence of the acquisition geometry, particularly in reconstructions of  
planes oblique to the plane of the detector. The study of the spatial resolution of oblique  
115 reconstructions is relevant to this application because the reconstruction of 3D images  
from a subset of projections may utilize a set of projections acquired at angles that are not  
symmetric about the source-detector axis. Additionally, oblique reconstructions may  
generally provide separate advantages for improving the visualization of features, such as  
microcalcifications.

120 A custom bench-top tomosynthesis system was used to acquire projections of a custom  
lead edge test-tool, which were then used to produce 3D reconstructions. The in-plane  
MTF was calculated from measured edge spread functions and the dependence of the  
MTF was measured with respect to the following factors: 1) the offset of the  
reconstruction plane from the plane containing the edge; 2) the obliquity of the  
125 reconstruction plane with respect to the detector; 3) the number of projections per  
reconstruction; and 4) the acquisition's angular range. Findings were validated by  
developing an analytical model of the MTF (accounting for blurring due to focal spot  
size, magnification, reconstruction pixel size, out-of-focus plane, and reconstruction  
blurring) and by replicating the experiment on a clinical tomosynthesis system.

## 130 II. METHODS

### A. Image acquisition

Projection images were acquired using a custom x-ray imaging testing station with x-ray source, detector, rotary stage, and filter as shown in Figure 2. The testing station uses a GE Senographe 500 x-ray generator (General Electric Health Care, Chalfont-St. Giles, UK) with a selenium flat-panel detector (Direct Radiography Corp, Newark, DE). Parker Motion stepper motors (Parker Hannifin, Rohnert Park, CA) are used to drive a rotary stage on which a phantom can be mounted and rotated, as well as a custom filter wheel; magnetic sensors are used to precisely control the position of the rotary stage and filter wheel. The filter wheel is laser-cut acrylic with various mounted filter metals, including 0.5 mm of aluminum used in this experiment. Additionally, the x-ray tube has a 25  $\mu\text{m}$  molybdenum filter mounted to the exit port.

For the purpose of describing our methods, we define an origin axis as the line between the center of the focal spot and the detector that intersects the detector at a right angle. In this testing station, the source and detector are stationary and the test object moves by rotation of the rotary stage (the rotary stage is centered on the origin axis such that rotation of the test object is equivalent to rotation of the x-ray tube and detector around the axis of the test object). This simulates an acquisition procedure in which the source and the detector move around the subject; for the purposes of describing our methods, the term "angular range" will be used to describe the rotation of the test object during image acquisition. The components of the testing station are coordinated by software written in C (Visual Studio 2010, Microsoft, Redmond, WA) which allows the user to control the

x-ray exposure parameters, filter wheel setting, acquisition geometry parameters, detector acquisition time, and the acquisition itself.

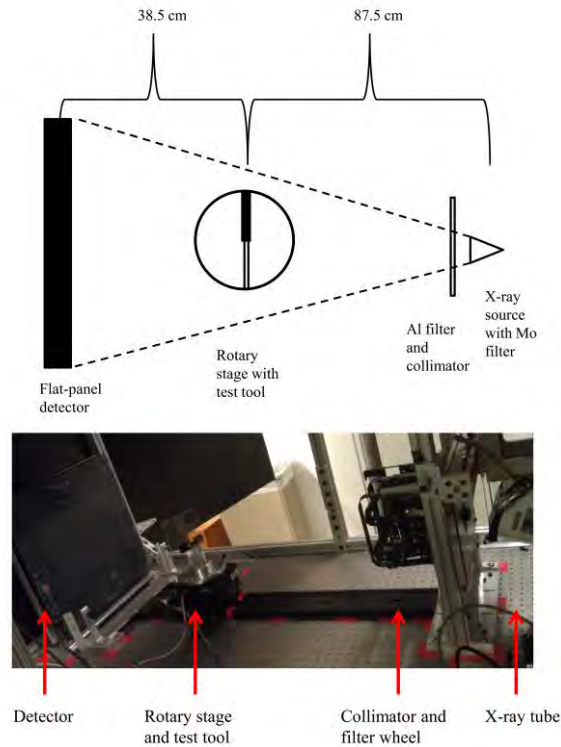
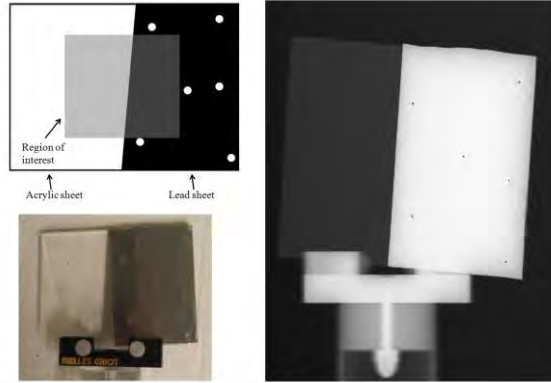


**Figure 2:** (top) The upper image depicts a schematic of custom x-ray imaging station from aerial view. An x-ray source, aluminum filter, and rotary stage with test object are positioned in succession in front of a flat panel detector. (bottom) The image below is a photograph of the x-ray testing station (filter wheel is not visible).

Projections were acquired using 32 kV and 83 mAs exposures through an aluminum filter of 0.5 mm thickness and a molybdenum filter of 25  $\mu\text{m}$ . Unless otherwise stated, 17 projections were acquired with an angular range of  $\pm 16^\circ$ , each at an interval of  $2^\circ$ . The exposure was collimated to the size of the object being imaged, in order to reduce scatter. Backprojection filtering was used to reconstruct the images (Briona, Real Time Tomography LLC, Villanova, PA).



165

**Figure 3:** (left top) Schematic of lead edge test tool used for assessment of spatial resolution. The grey region is a sample region of interest used for calculation of the edge spread function. (right) Sample image of reconstruction in the plane of the lead edge. (left bottom) Photo of lead edge test tool.

170 A test tool consisting of a 0.250 mm thick lead edge affixed to a 5.88 mm acrylic sheet was imaged on the system, designed as shown in Figure 3. The edge is tilted at a  $3^\circ$  angle and has six small holes of approximately 1 mm diameter to assist in obtaining the correct oblique reconstruction plane for modulation transfer function analysis and to calibrate the relationship between pixels and physical distance in the reconstruction plane.

## 175 **B. Modulation Transfer Function (MTF)**

The MTF is computed using the algorithm described by Carton *et al.*<sup>6</sup>. For the tomosynthesis reconstructions, the MTF is computed by taking the MTF of an edge in a slice of the reconstruction. Briefly, the procedure is as follows:

1. A rectangular region of interest (of 750 x 350 pixels or 80.3 x 37.5 mm) including the edge is selected.
2. A derivative filter is used to find the edge.

180



3. The edge is interpolated and a super-sampled edge spread function (ESF) is computed over the ROI using a sliding window with a sub-region column size of 20.
- 185 4. A monotonic filter is used to reduce the noise of the ESF<sup>7</sup>.
5. The line spread function (LSF) is computed by differentiation of the ESF with a differentiation kernel of  $[-1 \ 1]$  and correction for finite element differentiation.
6. The MTF is computed by taking the Fourier transform of the LSF.

## C. Experiments

### 190 1. Variation of MTF with reconstruction slice offset

The effect of the reconstruction slice offset relative to the plane that contains the edge was measured by obtaining reconstruction slices in 0.1 mm increments from the true slice depth containing the edge. The MTF of the same region of interest encompassing part of the test tool as described previously in section B of the Methods was measured in each  
195 image. The projections for these reconstructions are centered around the origin axis, in which the lead sheet is parallel to the detector in the central projection angle (the edge was rotated from  $-16^\circ$  to  $16^\circ$  in  $2^\circ$  increments).

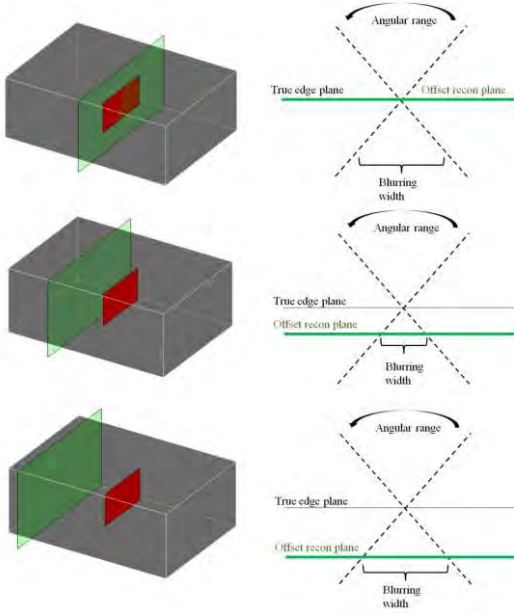


**Figure 4:** (left) Graphical depiction of the process by which the MTF is analyzed at each increasing reconstruction slice offset, in which a feature of interest is in the smaller (red) plane and the reconstruction plane is shown as the larger (green) plane. (right) Graphical depiction of the intersection of the projections at the plane containing a feature of interest and the reconstruction plane.

This procedure is depicted graphically in Figure 4, in which the gray cube represents a volume of tomosynthesis data, a feature of interest is located in the smaller (red) plane, and the larger (green) reconstruction plane is offset from the plane containing the feature of interest by various distances and the MTF measured at each offset. All MTF data are corrected as will be described in section C4 of the Methods. The diagrams on the right of Figure 4 show where the projections intersect the plane containing the edge and the reconstruction plane (this diagram will be elaborated upon in section C4 of the Methods).

## **2. Variation of MTF with oblique reconstruction angle**

The effect of the reconstruction slice angle in an oblique reconstruction on the MTF was  
215 assessed by changing the angle of the lead sheet with respect to the detector in the  
reconstruction. This was done by obtaining projections of the test tool in which the  
central projection was not one in which the test tool was parallel to the detector. The  
MTF was computed for the same ROI at different depths for each obliquely angled  
reconstruction. The MTF for each reconstruction slice angle was taken as the curve with  
220 the greatest overall MTF for each of the different depths at that angle. This maximum  
MTF of a group of MTFs was computed by smoothing the data and looking for the curve  
with the highest frequency at which the MTF drops to 50%. All MTF data are corrected  
as will be described in section C4 of the Methods.

## **3. Variation of MTF with the number of projections**

225 The effect of the number of projections used to create a reconstruction on the MTF was  
assessed by reducing the number of projections to a subset of the 17 acquired projections.  
In one experiment, the angular range of acquisition was maintained at  $\pm 16^\circ$  while the  
angular spacing between projections was increased. Projection subsets of size 15, 13, 11,  
and 9 were examined. In another experiment, the angular range was reduced to  $\pm 14^\circ$ ,  
230  $\pm 12^\circ$ ,  $\pm 10^\circ$ , and  $\pm 8^\circ$  while maintaining the angular spacing between projections (and the  
projection subset size reduced accordingly for each experiment). All MTFs are corrected  
as will be described in section C4 of the Methods.

#### 4. MTF Simulation

We hypothesized that the decay of the MTF with respect to reconstruction slice offset  
235 results from a combination of image blurring due to the size of the reconstruction pixels,  
blurring due to the offset of the reconstruction slice to the true slice that contains the  
edge, the blurring due to the reconstruction process, and the blurring due to the focal spot  
and geometric properties of the imaging system. It should be noted that the MTF is  
known to exhibit degradation due to the oblique incidence angle of x-rays on the  
240 detector<sup>8-15</sup>. However, because the detector used in this experiment is selenium based, the  
MTF degradation due to this effect is assumed to be close to zero and is not modeled<sup>16</sup>.  
The combination of all of the above mentioned blurring factors can be modeled as a  
convolution of rect functions in the spatial domain, or a multiplication of sinc functions  
in the frequency domain<sup>17</sup>.

245 In the following equations,  $x$  = position (mm),  $f$  = spatial frequency ( $\text{mm}^{-1}$ ),  $p$  = pixel size  
in the reconstruction ( $\mu\text{m}$ ),  $d$  = reconstruction slice offset (mm),  $\theta$  = half of the angular  
range (degrees),  $m$  = geometric magnification,  $a$  = width of the Gaussian focal spot  
distribution (mm),  $M_p$  = MTF of a single projection image parallel to the detector,  $M_r$  =  
MTF of a reconstruction slice where the central angle has the edge parallel to the  
250 detector, and "\*" is the scalar multiplication operator (see Figure 5 for a graphical  
depiction of geometric terms). The blurring due to the reconstruction slice offset can be  
modeled as a rect function with width equal to the width of the shadow cast by the feature  
of interest onto the reconstruction plane, or the value of  $2b$  in Figure 5.

$$\text{LSF}_{\text{offset}}(x) = \text{rect}\left(\frac{x}{2d \tan(\theta)}\right) \quad (1)$$

255 The blurring due to the size of the reconstruction pixels is also modeled as a rect function with width equal to the pixel size in the reconstruction plane<sup>18-20</sup>.

$$\text{LSF}_{\text{detector}}(x) = \text{rect}\left(\frac{x}{p}\right) \quad (2)$$

The blurring due to the reconstruction process was modeled by dividing the MTF of a reconstruction in the plane of the edge at 0 mm slice offset by the MTF of the central  
260 projection image acquired in the direction of the origin axis. The same projection is used for all simulated blurring due to reconstruction.

$$\text{MTF}_{\text{reconstruction}}(f) = \frac{M_r}{M_p} \quad (3)$$

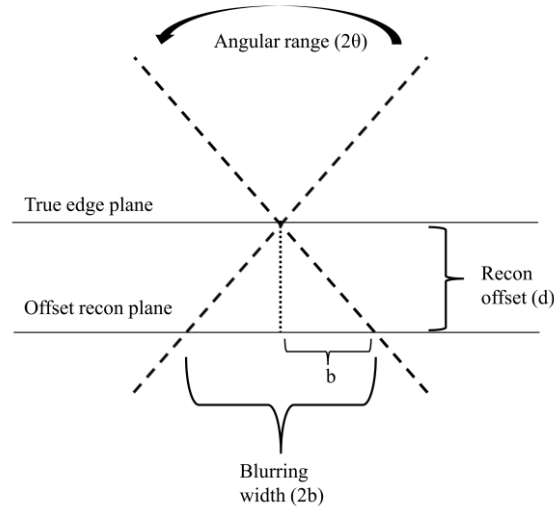
The blurring due to the focal spot size was modeled as described by Siewerdsen and Jaffray in 2000<sup>21</sup>.

$$265 \quad \text{MTF}_{\text{focal spot}}(f) = (e^{-\pi * \frac{m-1}{m} * a * f})^2 \quad (4)$$

Taking the Fourier transforms of  $\text{LSF}_{\text{offset}}$  and  $\text{LSF}_{\text{detector}}$  (ignoring the resulting coefficient in order to normalize the maximum value to 1) and multiplying all four factors together results in the following equation for the MTF of a specific reconstruction slice offset from the true edge plane and a specific angular range:

$$270 \quad \text{MTF}(f) = |\text{sinc}(\pi f p)| * |\text{sinc}(2\pi f d \tan(\theta))| * \frac{M_r}{M_p} * (e^{-\pi * \frac{m-1}{m} * a * f})^2 \quad (5)$$

As illustrated in Figure 5, we expect that the blurring is due in part to the offset of the reconstruction plane from the true plane containing the edge, which causes the projections passing through the edge to cast a magnified shadow onto the reconstruction plane.



275

**Figure 5:** Depiction of the blurring due to an offset of the reconstruction plane from the true plane that contains the edge based on the angular range of acquisition.

In the acquisitions described in sections C1, C2, and C3 of the Methods, a low frequency  
 280 artifact was observed in the in-plane MTF measured from their reconstructions. It is  
 hypothesized that this artifact was due to non-linearity in the detector, which is an older,  
 selenium-based detector (the possible sources of this artifact will be described in more  
 detail in the Discussion). This artifact is depicted in Figure 6 below, where the MTF data  
 at 83 mAs and 0 mm reconstruction slice offset is superimposed against a simulated MTF  
 285 curve at 0 mm reconstruction slice offset (using the equation described above) in which  
 the artifact is absent.

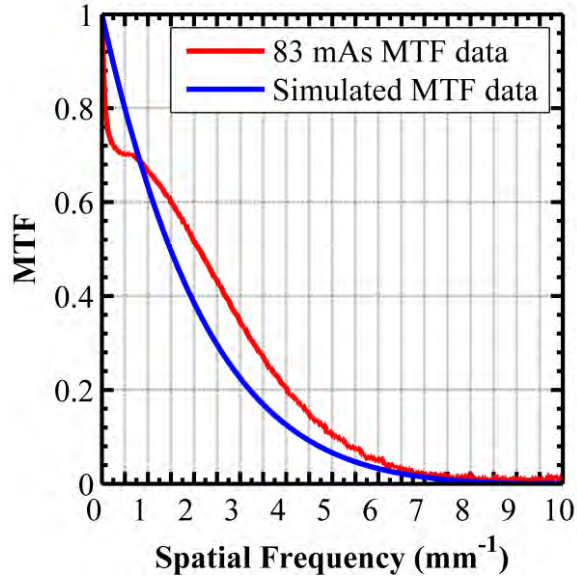
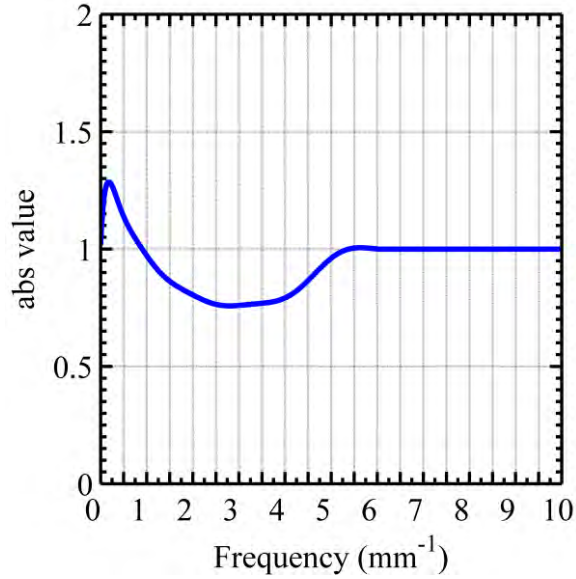


**Figure 6:** Simulated MTF data at 0 mm slice offset superimposed with actual 83 mAs MTF data at 0 mm slice offset. A low frequency artifact is visible in the actual data, as well as some offset in the corresponding MTF values.

290

The quotient of the simulated MTF with no slice offset and the actual MTF with no slice offset was computed, smoothed (for all values at greater than  $6 \text{ mm}^{-1}$  spatial frequency, the data was set to 1 due to the low signal of the MTF data), and used as a correction factor (see Figure 7); assuming the correctness of the simulation, this quotient would represent only the artifact and it should be valid to apply this correction factor to MTF data at all slice offsets.

295



300 **Figure 7:** The quotient of the simulated MTF with no slice offset and the actual MTF  
with no slice offset.

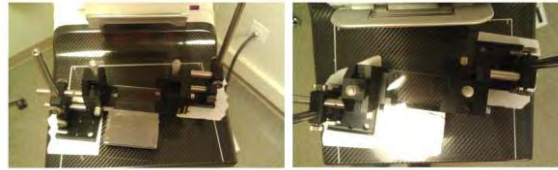
The experimental MTF at all slice offsets was adjusted by multiplication by this  
correction factor obtained at 0 mm offset. If the factors included in the simulation are  
305 accurate, it can be expected that this operation would effectively eliminate the low  
frequency artifact at all slice offsets, as well as in reconstructions with different angular  
ranges.

## 5. Experimental validation with a clinical system

310 In order to validate the MTF measurements seen in reconstructions at different slice  
depths on the RTT system, a similar experiment was conducted to observe the change in  
MTF with reconstruction slice offset on a clinical Selenia Dimensions (Hologic, Bedford,  
MA) tomosynthesis system. The Hologic system reconstructs slices between the detector  
and the breast support in 1 mm increments, where the detector and breast support are



315 parallel. In order to replicate the effect of changing the reconstruction slice depth at smaller increments, a fixture was designed to elevate the test tool between the detector and the breast support. The experimental setup is shown in Figure 8.



320 **Figure 8:** Experimental setup to measure MTF in planes offset from the plane of the lead edge on a clinical Hologic tomosynthesis system.

The Hologic tomosynthesis system has an angular range of  $\pm 7.5^\circ$  and acquires a projection every  $1.07^\circ$ . The images were produced using 32 kV and 6 mAs for each projection. The test tool was moved in  $100\ \mu\text{m}$  increments for 2 mm, in order to traverse the distance equivalent to three adjacent reconstruction slices (which are spaced in 1 mm steps). The MTF was measured using the technique detailed in section B of the Methods. Measurements were made for several reconstruction slices as the test tool was translated along the origin axis. We expected to see results concordant with the experiment detailed in section C.1 of the Methods, in which the reconstruction slice offset was increased in  $100\ \mu\text{m}$  increments.

### 330 **III. RESULTS**

#### **A. Variation of MTF with reconstruction slice offset**

Figure 9 shows the change in the MTF as the reconstruction slice offset is changed. Each MTF is computed from a region of interest of size 750 pixels by 350 pixels (80.3 mm x

37.5 mm). It can be seen that the MTF with the least decay is from the plane that contains  
 335 the true position of the edge (0 mm offset). As the reconstruction plane deviates from the  
 true plane, the MTF decays increasingly. The MTF decay appears to be symmetric with  
 respect to positive and negative position offsets of the reconstruction plane.

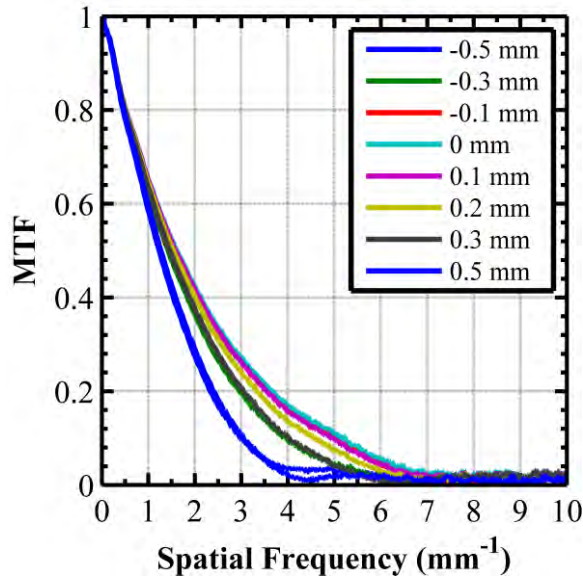
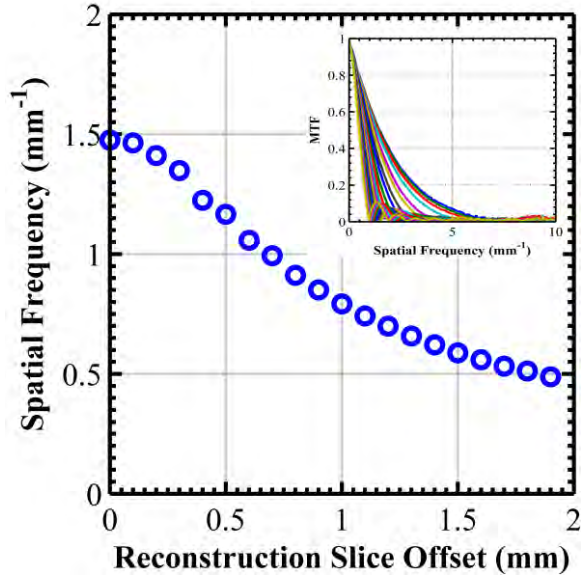


**Figure 9:** MTF versus frequency of reconstruction slices of the test tool in the plane of  
 340 the edge, at several selected offsets from the plane containing the edge. As the curves  
 transition from superior to inferior, the reconstruction slice offset is increased from 0 to  
 0.5 mm. It can be observed that the MTF decays as the reconstruction plane is further  
 removed from the plane containing the edge and that offset in either direction is  
 symmetric in the MTF.

345

The spatial frequency at which the MTF at each reconstruction slice offset (over a range  
 of 0-2 mm) drops to 50% of its maximum value is plotted in Figure 10, in order to better  
 depict the rate of degradation.



350 **Figure 10:** The spatial frequency at which the MTF drops to 50% of its maximum value versus the reconstruction slice offset over a 0-2 mm range of slice offsets, in 0.1 mm increments. The pictograph in the upper right corner shows the original MTF data for this set of reconstruction slice offsets.

## 355 **B. Variation of MTF with oblique reconstruction angle**

It was observed that the MTF changes slightly as the obliquity of the reconstruction plane is increased. Figure 11 shows the distribution of MTFs across a 64° range of reconstruction slice angles (-32° to 32° with respect to the plane parallel with the detector, in 2° increments). There exists a distinct trend in the data showing that the MTF degrades as the obliquity of the reconstruction plane increases, shown in Figure 11 by the transition from superior to inferior curves (blue to red). One outlier was removed from this dataset.

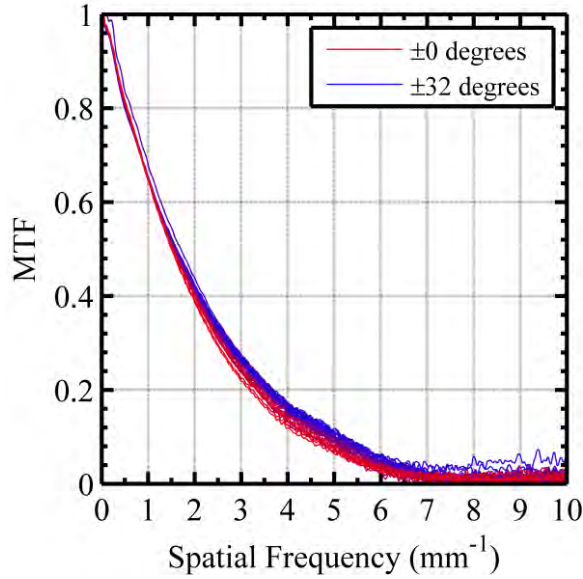


**Figure 11:** MTF versus frequency for a range of reconstruction slice angles in which the lead edge is positioned in the plane for each reconstruction. The MTF curves transition from blue to red as the obliquity of the reconstruction slice angle increases. A clear trend is visible that shows the MTF degrading slightly as the obliquity increases (from the superior to the inferior curves).

To illustrate this trend further, the frequency at which the MTF drops below 50% of its maximum value is plotted for each of the 33 different reconstruction slice angles in Figure 12. The trend is clearly visible in this figure.

A second order polynomial fit was plotted through this data as shown in Figure 12. In an ideal system, the peak of the hyperbola would be located at  $0^\circ$ , but some outliers and noise exist in the data. Figure 12 shows that the MTF drops by 4.1% when comparing the peak MTF to the MTF at a  $32^\circ$  obliquity from the peak, based on the trendline data.

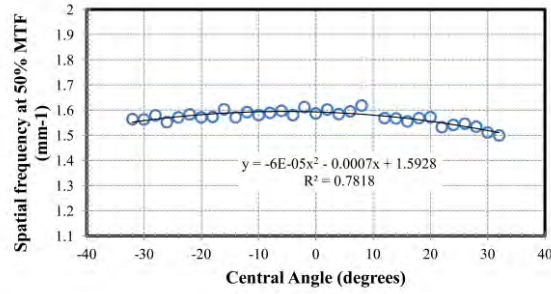


**Figure 12:** Polynomial fit through 50% of maximum MTF data for each central angle. The fitted data has equation displayed above with an  $R^2$  value of 0.7818.

380

### C. Variation of MTF with the number of projections

Based on the analytical model described in section C4 of the Methods, we hypothesized that changing the number of projections and preserving the angular range of acquisition would not have an effect on the MTF. Figure 13 shows the MTF in the plane of the test  
 385 tool for a varying number of projections used to create the reconstruction. There is little change in the MTF as the number of projections changes, and there is no distinguishable trend so long as the angular range remains the same. This appears to be true regardless of which  $n$  projections are used to reconstruct a subset of size  $n$ ; that is, given a set of 17 projections, a reconstruction using any 5 of them will produce the same MTF as if all 17  
 390 projections were used in the reconstruction, provided the outer-most projection angles are included in the five.

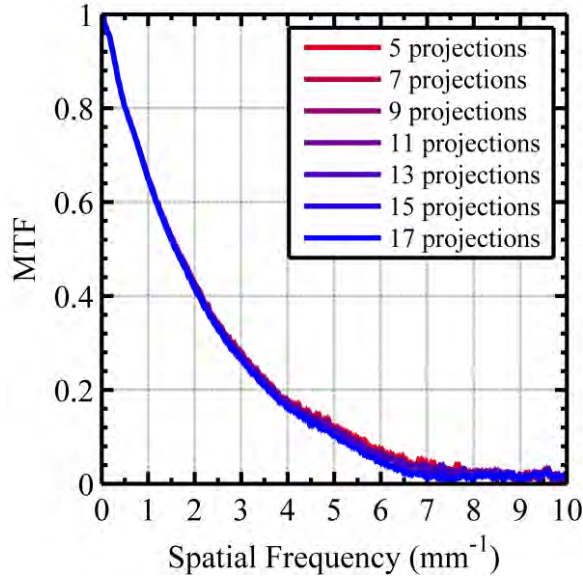
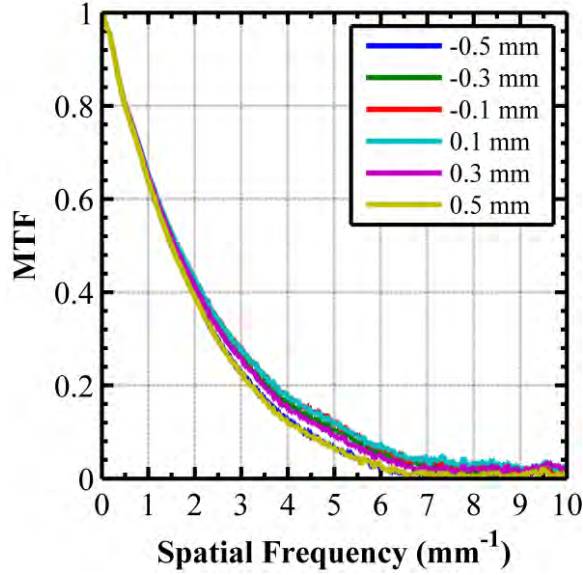


**Figure 13:** MTF versus frequency for reconstructions in the plane of the lead edge created using varying numbers of projections.

395

Based on the analytical model described in section 4 of the Methods, we hypothesized that the MTF would degrade at a slower rate with respect to the reconstruction slice offset if the angular range was reduced, due to a reduced contribution to blurring. As the angular range of acquisition decreases, the MTF decays more slowly with respect to the reconstruction slice depth. Figure 14 shows the MTF as the reconstruction slice depth deviates from the plane containing the edge, in a reconstruction with 9 projections and an angular range of  $\pm 8^\circ$  (50% of full angular range). It can be observed that the amplitude of the MTF decays more slowly than in reconstructions with a larger angular range.

400



405

**Figure 14:** MTF versus frequency for a reconstruction with 9 projections and an angular range of  $\pm 8^\circ$ , varied over several reconstruction slice depths. The reconstruction slice offset is increased as the curves transition from superior to inferior.

It then follows that the MTF degradation with respect to reconstruction slice offset should  
 410 remain the same if the angular range is preserved and any number of projections is used  
 in the reconstruction. As can be seen in Figure 15, when the angular range is kept  
 constant while the number of projections is reduced, the MTF decays similarly with  
 reconstruction depth as when the full set of projections is used. Figure 15 shows the  
 variation of MTF with reconstruction slice depth in a reconstruction from 9 projections  
 415 with an angular range of  $\pm 16^\circ$ , and this figure is analogous to Figure 8, in which all 17  
 projections are used in the reconstruction.

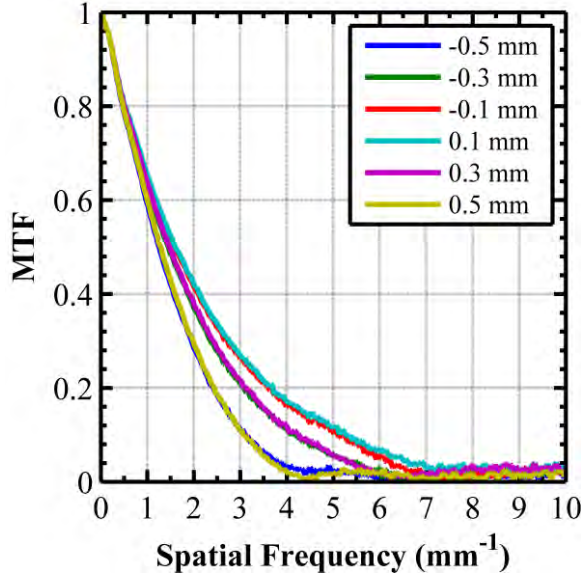


**Figure 15:** MTF versus frequency at different reconstruction slice depths with a reconstruction created from 9 projections and an angular range of  $\pm 16^\circ$ . It can be observed that the decay of the MTF is very similar to that seen in a reconstruction with the same angular range but more projections. The reconstruction slice offset is increased as the curves transition from superior to inferior.

#### D. MTF Simulation

In order to gain a better understanding of the sources of blurring in the MTF, an analytical model of the MTF was developed which composed all of the understood components of blurring as described in section 4 of the Methods. Figure 16 shows the results of this analytical model for an angular range of  $\pm 16^\circ$  and reconstruction slice offsets ranging from 0 to 1.9 mm. The analytical model shows an MTF similar to actual MTF data under the given parameters, and with similar degradation properties as the actual MTF data. Although the simulated data is very well aligned with the experimental data, the alignment is not perfect, owing to the lack of full understanding of the mechanisms of blurring in tomosynthesis. It should be noted that experimental data at all



depths in Figure 16 were corrected by the same correction factor shown in Figure 6.

435 Despite this correction for the artifact caused by hardware limitations, some misalignment between the simulated and the experimental data exists, likely due to sources of blurring that are not yet well understood.

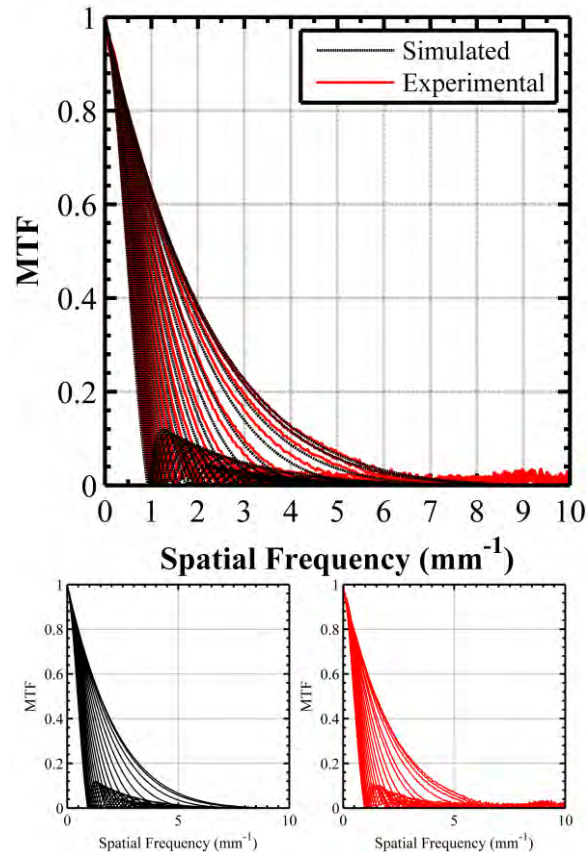
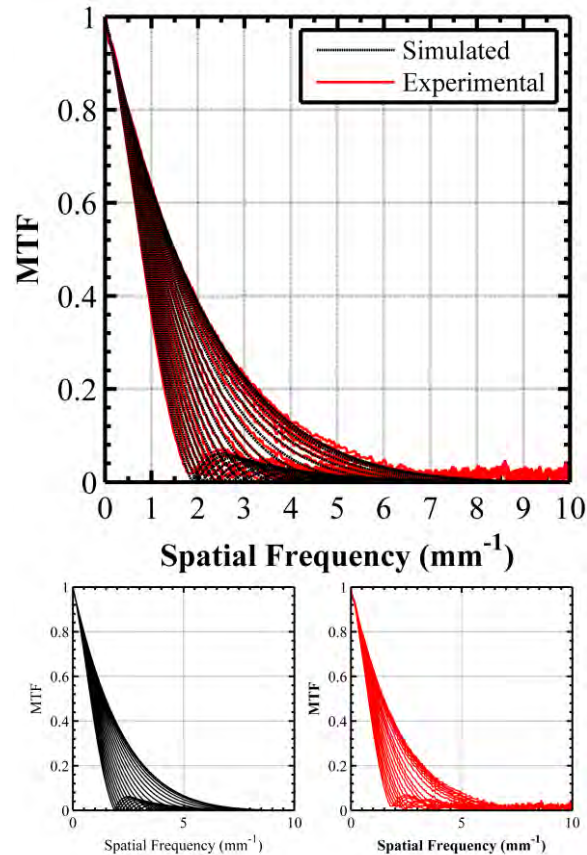


**Figure 16:** (top) The results of the analytical model of the MTF (red) superimposed against an actual MTF dataset acquired from the test tool (black), both over a range of reconstruction slice offsets from 0 to 1.9 mm in 0.1 mm steps with  $\pm 16^\circ$  angular range. (bottom left) The simulation results for this range of slice offsets, plotted alone. (bottom right) The experimental MTF for this range of slice offsets, plotted alone. The superior curves are for a slice offset of 0 mm and the inferior curves are for a slice offset of 1.9 mm.

440  
445

In addition to simulating the effect of increasing the reconstruction slice offset at  $\pm 16^\circ$  angular range, a simulation of this effect at  $\pm 8^\circ$  angular was also performed and compared

to an actual dataset, illustrated in Figure 17. This simulation reflected the rate of degradation of the actual data nicely, but once again, the data was not perfectly aligned.



450

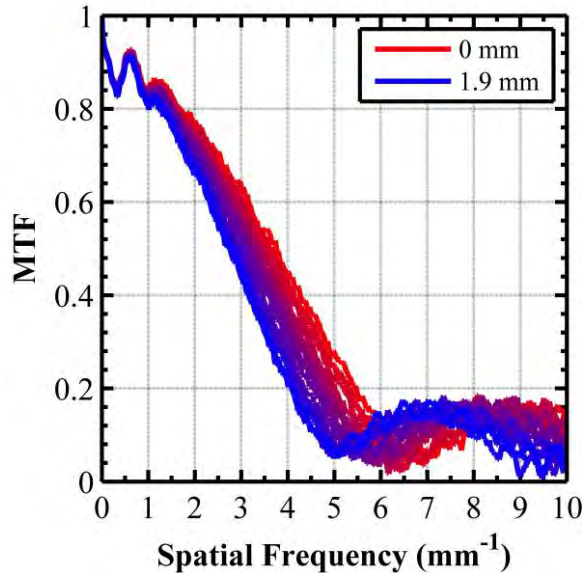
**Figure 17:** (top) The results of the analytical model of the MTF (red) superimposed against an actual MTF dataset acquired from the lead edge test tool (black), both over a range of reconstruction slice offsets from 0 to 1.9 mm with  $\pm 8^\circ$  angular range. (bottom left) The simulation results for this range of slice offsets, plotted alone. (bottom right) The experimental MTF for this range of slice offsets, plotted alone. The superior curves are for a slice offset of 0 mm and the inferior curves are for a slice offset of 1.9 mm.

455

## E. Experimental validation with a clinical system

460 The same trend of decaying MTF with increasing reconstruction slice offset is visible in a repetition of the experiment on a clinical Hologic system. Figure 18 shows the MTF

versus frequency for several instances of a single reconstruction slice in which the test tool is moved away from the slice containing the edge in 100  $\mu\text{m}$  increments.



465 **Figure 18:** MTF versus frequency in Hologic tomosynthesis reconstructions where the lead edge is moved away from the reconstruction slice that contains the edge. The MTF can be seen to decay as the slice moves further from the slice containing the edge (as the curves transition from superior, red, to inferior, blue).

470 Figure 18 appears to show a consistent degradation in the MTF as the offset of the reconstruction plane from the plane containing the test tool increases. In order to better visualize the characteristics of the degradation with increasing slice offset, the frequency at which the MTF drops below 50% of maximum is plotted for each reconstruction slice offset in Figure 19, showing a largely linear degradation over the 2 mm range. Compared to Figure 9, it is hypothesized that this data is still degrading in the linear range, analogous to the 0 mm - 0.25 mm slice offset range of Figure 9. For clinical purposes, the Hologic system generates reconstruction slices at 1 mm increments, and thus, the

maximum offset of the closest reconstruction plane to a feature of interest never exceeds  
 480 0.5 mm, at which there is a maximum MTF degradation of only 9%.

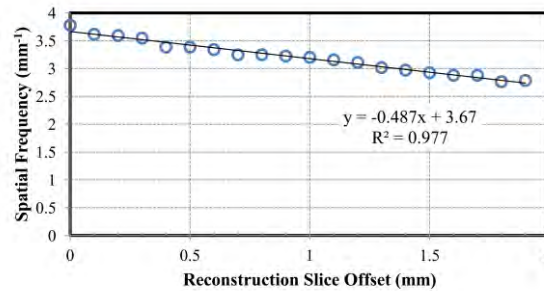


**Figure 19:** Reconstruction slice offset versus spatial frequency at which the MTF drops  
 below 50% of maximum. This data is fit linearly (with an  $R^2$  value of 0.977) and appears  
 to follow such a linear degradation as the reconstruction plane moves away from the  
 485 plane containing the feature of interest over a 2 mm range.

## IV. DISCUSSION

### A. Consequences of this work

#### 1. Effect of slice alignment on the conspicuity of clinical features

490 Blurring of features in a tomographic image is a non-trivial problem that is not present in  
 mammography or stereomammography. In the case of mammography, the attenuation of  
 a feature of any depth or thickness is projected directly onto the image plane, whereas a  
 tomographic reconstruction interrogates a volume of data in which features are located in  
 certain planes depending on the thickness of the feature. Features of small thickness  
 495 along the detector-source axis but with high attenuation which are readily visible in  
 mammographic images may be completely absent from tomographic reconstructions due  
 to the additional blurring factors associated with tomosynthesis. This has a serious impact  
 on the use of breast tomosynthesis in a clinical setting.

Multiple clinical studies have reported that tomosynthesis is limited in its ability to detect  
500 breast microcalcifications. Calcifications in breast tissue are indicative of local cell death  
or secretions due to pathological activity and can be precursors to breast cancers such as  
ductal carcinoma<sup>22, 23</sup>. Breast microcalcifications are often 100-300  $\mu\text{m}$  in thickness,  
whereas tomographic reconstruction slice spacings are often placed at a 500-1000  $\mu\text{m}$   
offset. Given a 300  $\mu\text{m}$  calcification and a 1000  $\mu\text{m}$  slice spacing, there is a 70% chance  
505 that a random set of slices with 1000  $\mu\text{m}$  spacing will not have a single slice that passes  
through the calcification. The calcification may still be visible in planes offset from the  
actual position of the calcification, but the spatial resolution will be degraded due to  
blurring. The results presented in this work may help determine tolerable reconstruction  
offsets, and hence, the minimum slice spacing which retains sufficient spatial resolution  
510 to depict small clinical features such as microcalcifications.

The sources of blurring in tomosynthesis are not fully understood. It can be interpreted  
from the results of this work that blurring is at least partially due to a combination of: 1)  
the offset of the reconstruction plane from the plane containing the feature; 2) the angular  
range of the acquisition; 3) the detector element and source properties; and 4) the  
515 acquisition geometry. As illustrated in Figure 4, when the offset of the reconstruction  
plane from the feature increases, the feature projects a larger and more blurred shadow  
onto the reconstruction plane. This effect can be characterized by the degradation of the  
MTF of an edge as the edge moves away from the reconstruction plane, as can be seen in  
Figure 8. The degradation is quite severe in a system which uses a  $\pm 16^\circ$  angular range of  
520 acquisition as demonstrated in section A of the Results. In reconstructions with an

angular range of  $\pm 16^\circ$ , the frequency at which the MTF drops to half of its maximum value occurs at about a 600  $\mu\text{m}$  offset of the reconstruction plane. On the other hand, when the angular range is reduced to  $\pm 8^\circ$ , the MTF dropoff with slice offset is much less steep, as depicted in Figure 14.

525 The rate of increase of the blurring with increasing distance between the feature and the reconstruction plane is due in part to the angular range of acquisition. When the angular range of an acquisition is increased, the tomographic ability (or the ability to resolve characteristics of features in three dimensions) of the reconstruction is increased<sup>24</sup>. As illustrated in Figure 3, for a single reconstruction plane with some offset, as the acquisition's angular range increases, the shadow projected by the feature onto the plane  
530 widens, representing an increase in blurring. Likewise, as illustrated in Figures 14 and 15, decreasing the angular range decreases the rate at which blurring increases due to the reconstruction slice offset. These results are in line with the observations of Maidment *et al.* (2005), who noted that using a smaller range of projection angles results in less  
535 blurring of out of plane structures, and who determined a relationship between resolution at the limiting frequency and angular range in tomosynthesis images<sup>25</sup>. Thus, increasing the angular range increases the need for accurate slice spacing as features will become out-of-focus even with small changes in reconstruction plane depth. Practically, the selection of the angular range represents a trade-off between accurate localization of an  
540 existing feature in the detector-source axis (e.g. characterization of the size and location of an existing calcification) and ease of screening for features in a three-dimensional space (e.g. screening tomographic reconstructions to search for microcalcifications).

Interestingly, the number of projections per reconstruction did not affect the MTF so long as the reconstruction plane offset and the acquisition's angular range were held constant, as shown in Figure 15. This knowledge could potentially be used to reduce the radiation dosage during tomosynthesis if prior knowledge of the structure being imaged exists and the known features do not require high resolution between the sparsely spaced views. For example, this technique is particularly applicable for needle tracking during biopsy procedures. Based on the position of the needle and the tissue, projection views at certain time points may have obstructions that block the view of the feature or may not contain useful geometric information. Selectively reconstructing images from certain projections based on this knowledge could improve temporal resolution or reduce radiation dose. However, decreasing the number of projections per reconstruction can lead to obvious artifacts from high contrast features. Small numbers of projections with high-contrast features generate artifacts in reconstructions, which are blurred and made less obvious as the number of projections increases. Increasing the number of projections per reconstruction distributes the intensity of high contrast features over several components and causes artifacts to be less obvious.

## **2. Anisotropy of resolution**

It is well known that tomosynthesis produces images with anisotropic spatial resolution, due to the limited angular range of acquisition<sup>26</sup>. The present work further illustrates the anisotropic nature of spatial resolution in tomosynthesis as objects move in and out of focus. The characterization of this blurring based on the aforementioned factors can allow for the estimation of the appropriate reconstruction slice spacing for a particular clinical

565 problem. In order to resolve small clinical features with an acceptable spatial resolution, finer reconstruction slice spacings may be necessary. Finer slice spacings would require storage of a larger amount of data or use of a dynamic reconstruction scheme in which slices can be recomputed from projection data dynamically based on a selected slice spacing<sup>27</sup>.

### 570 **3. Effect of obliquity on spatial resolution in tomosynthesis**

Acciavatti *et al.* (2012) have previously shown that digital breast tomosynthesis is capable of obliquely angled reconstructions<sup>28</sup>. Oblique reconstructions allow the visualization of surfaces that are not parallel to the detector, and have great potential in applications such as real-time imaging. For example, real-time three-dimensional  
575 tracking of a biopsy needle or other surgical tools is currently performed by careful insertion of the tool in a plane that is parallel to the detector. Oblique reconstruction would allow the alignment of the reconstruction slice with the tool in the image reconstruction procedure rather than by physical alignment of the tool during surgery. Additionally, oblique reconstructions may improve visualization of microcalcifications  
580 without increasing radiation dose.

The present work demonstrates that spatial resolution degrades minimally as the angular position of the reconstruction plane deviates from the angular position of the plane of the detector. The MTF can be used to characterize the in-plane spatial resolution of obliquely reconstructed planes. Figure 12 shows that the dropoff of the frequency value at which  
585 the MTF reaches 50% of the maximum MTF degrades at an increasing rate as the



obliquity increases. The maximum obliquity tested in this experiment was a plane angled at 32° to the plane of the detector. At this degree of obliquity, it was observed that the frequency value at which the MTF reaches 50% of the maximum fell by only about 10%, indicating that spatial resolution is relatively well preserved in oblique reconstructions.

590 This result indicates that reconstruction of oblique planes may be clinically acceptable.

## **B. Limitations of this work**

Reconstructions in this work were performed using backprojection filtering. The reconstruction algorithm supports super-resolution; that is, sub-pixel resolution<sup>29</sup>. Super-resolution has also been demonstrated to exist in iterative reconstructions<sup>30</sup>. The spatial

595 resolution characteristics of reconstructions computed by backprojection filtering and iterative reconstruction may be different, and the present work has not investigated the performance of iterative reconstruction. Lu *et al.* demonstrated the effect of voxel size on the in-plane intensity profile of iterative reconstructions with subpixel resolution<sup>31</sup>. Based on the concordance of backprojection filtering and iterative reconstruction super-

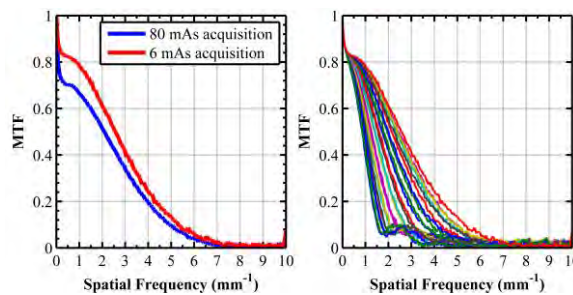
600 resolution results, it is likely that the factors affecting the MTF described in this work also apply to iterative reconstructions. However, exploring this relationship is outside of the scope of the present work.

Although not presented here, the effect of the reconstruction slice offset on the MTF in oblique reconstructions was examined and was found to be concordant with the MTF

605 degradation in non-oblique reconstructions (Figure 8 and section A of this work). The present work has not investigated the effect of the angular range of acquisition on the

degradation of spatial resolution with reconstruction slice offset in oblique reconstructions. This is a direction of interest that warrants future study.

The custom tomosynthesis system on which the experimental projections were acquired  
610 is a non-clinical "sandbox" system. It employs an older selenium flat-panel detector which is limited in its linear range. The MTF measurements of reconstructions from this system show a sharp drop in the 0-1  $\text{mm}^{-1}$ , which is an artifact of the detector being driven into nonlinear operation. Reducing the mAs during image acquisition can reduce this artifact but not entirely remove it. Figure 20 shows the MTF with variation in  
615 reconstruction slice offset of 0 mm to  $\pm 1$  mm with a 6 mAs acquisition (analogous to Figure 7). The intensity profile of the entire width of the test tool of the phantom was symmetric and reducing the field size by collimation did not affect the intensity profile, which ruled out scatter from the acrylic plate supporting the lead edge as only one side of the lead edge was adjacent to the acrylic.



620

**Figure 20:** (left) Comparison of MTF between 80 mAs acquisition and 6 mAs acquisition. The low mAs acquisition shows a much smaller non-linearity artifact at low frequency, suggesting that this artifact may be due to detector limitations. (right) Example of MTF data with variation in reconstruction slice offset at low mAs at  
625 reconstruction slice offset of 0 mm to  $\pm 1$  mm.

## **V. CONCLUSION**

The MTF of tomosynthesis systems is spatially anisotropic and varies with sub-slice spacing. Angular range and slice alignment both contribute to the blurring that causes degradation of the in-plane MTF. This blurring, due to sub-slice misalignment of objects, may adversely affect the conspicuity of small clinical features such as microcalcifications and may require finer slice spacing and the storage of an increased amount of data. An increase in the angular range of acquisition also contributes to blurring but improves tomographic ability. Additionally, reconstruction of oblique planes results in minimal degradation of the MTF and thus may be clinically acceptable. It is evident that many factors affect blurring and image quality and that careful deliberation on each factor and tradeoff may be necessary to best identify certain clinical features in both 3D and 4D tomosynthesis.

## **VI. ACKNOWLEDGEMENTS**

This work was supported in part by U.S. Army Medical Research and Materiel Command Grant W81XWH-11-1-0229, “Dynamic Contrast-Enhanced Digital Breast Tomosynthesis”. The views, opinions and/or findings contained in this report are those of the author and should not be construed as an official Department of the Army position, policy or decision. Additionally, I am grateful for the assistance of Yohei Matsutani. Assistance with image reconstruction was provided by Johnny Kuo and Susan Ng of Real-Time Tomography, LLC. Andrew Maidment is a member of the scientific advisory board of Real-Time Tomography.

## VII. BIBLIOGRAPHY

- <sup>1</sup>Drukteinis JS, Mooney BP, Flowers CI, Gatenby RA. (2013). Beyond Mammography:  
650 New Frontiers in Breast Cancer Screening. Am J Med, in press.
- <sup>2</sup>Gilles R, Meunier M, Lucidarme O, et al. (1996) Clustered breast microcalcifications:  
Evaluation by dynamic contrast-enhanced subtraction MRI. J Comput Assist  
Tomogr 20:9-14.
- <sup>3</sup>Westerhof JP, Fischer U, Moritz JD, et al. (1998) MR imaging of mammographically  
655 detected clustered microcalcifications: is there any value? Radiology 207:675-681.
- <sup>4</sup>Hylton N. (2005). Magnetic resonance imaging of the breast: opportunities to improve  
breast cancer management. American Society of Clinical Oncology. 23(8): 1678-1684.
- <sup>5</sup>Brown JM, Giaccia AJ. (1998). The unique physiology of solid tumors: opportunities  
(and problems) for cancer therapy. Cancer Research. 58(7): 1408-16.
- 660 <sup>6</sup>Carton AK, Vandenbroucke D, Struye L, Maidment A, Kao YH, Albert M, Bosmans H,  
Marchal G. (2005). Validation of MTF measurement for digital mammography quality  
control. Med Phys 32(6):1684-90.
- <sup>7</sup>Maidment A. D. A. and Albert M. (2003). "Conditioning data for calculation of the  
modulation transfer function," Med. Phys. 30, 248–253.
- 665 <sup>8</sup>Acciavatti RJ, Maidment AD. (2011). Optimization of phosphor-based detector design  
for oblique x-ray incidence in digital breast tomosynthesis. Medical Physics.  
38(11):6188-202.
- <sup>9</sup>Que W, Rowlands JA. X-ray imaging using amorphous selenium: Inherent spatial  
resolution. Medical Physics. 1995;22(4):365-74.

- 670 <sup>10</sup>Hajdok G, Cunningham IA. Penalty on the detective quantum efficiency from off-axis  
incident xrays. In: Yaffe MJ, Flynn MJ, editors. Medical Imaging 2004: Physics of  
Medical Imaging; 2004; San Diego, CA: SPIE; 2004. p. 109-18.
- <sup>11</sup>Mainprize JG, Bloomquist AK, Kempston MP, Yaffe MJ. Resolution at oblique  
incidence angles of a flat panel imager for breast tomosynthesis. Medical Physics.  
675 2006;33(9):3159-64.
- <sup>12</sup>Acciavatti RJ, Maidment ADA. Calculation of OTF, NPS, and DQE for Oblique X-Ray  
Incidence on Turbid Granular Phosphors. Lecture Notes in Computer Science.  
2010;6136:436-43.
- <sup>13</sup>Freed M, Park S, Badano A. A fast, angle-dependent, analytical model of CsI detector  
680 response for optimization of 3D x-ray breast imaging systems. Medical Physics.  
2010;37(6):2593-605.
- <sup>14</sup>Freed M, Park S, Badano A. Erratum: "A fast, angle-dependent, analytical model of CsI  
detector response for optimization of 3D x-ray breast imaging systems" [Med. Phys. 37,  
2593-2605 (2010)]. Medical Physics. 2011;38(4):2307.
- 685 <sup>15</sup>Badano A, Freed M, Fang Y. Oblique incidence effects in direct x-ray detectors: A  
first-order approximation using a physics-based analytical model. Medical Physics.  
2011;38(4):2095-8.
- <sup>16</sup>Lee DL, Cheung LK, Rodricks B, Powell GF. (1998). Improved imaging performance  
of a 14 x 17-inch Direct Radiography (TM) System using Se/TFT detector. In: James T.  
690 Dobbins I, Boone JM, editors. SPIE Conference on Physics of Medical Imaging; San  
Diego, CA p. 14-23.

- <sup>17</sup>Boyce SJ, Samei E. (2006). Imaging properties of digital magnification radiography. Med Phys 33(4): 984-996.
- <sup>18</sup>M. Albert and A. D. A. Maidment, "Linear response theory for detectors consisting of  
695 discrete arrays," Med. Phys. 27(10), 2417-2434 (2000).
- <sup>19</sup>R. J. Acciavatti and A. D. A. Maidment, "An analytical model of NPS and DQE comparing photon counting and energy integrating detectors," in SPIE Medical Imaging, edited by E. Samei and N. J. Pelc (SPIE, San Diego, CA, 2010), pp. 76220I-1 - 76220I-12.
- 700 <sup>20</sup>R. J. Acciavatti and A. D. A. Maidment, "A comparative analysis of OTF, NPS, and DQE in energy integrating and photon counting digital x-ray detectors," Med. Phys. 37(12), 6480-6495 (2010).
- <sup>21</sup>Siewerdsen JH, Jaffray DA. (2000). Optimization of x-ray imaging geometry (with specific application to flat-panel cone-beam computed tomography). Med Phys. 27(6):  
705 1311-1323.
- <sup>22</sup>Robbins and Cotran. (2009). Pathological Basis of Disease, 8th edition, Elsevier.
- <sup>23</sup>Ernster VL, Ballard-Barbash R, Barlow WE, et al. (2002). Detection of ductal carcinoma in situ in women undergoing screening mammography. Journal of the National Cancer Institute. 94(20): 1546-54.
- 710 <sup>24</sup>Park JM, Franken EA, Garg M, Fajardo LL, Niklason LT. (2007). Breast Tomosynthesis: Present Considerations and Future Applications. RSNA RadioGraphics. 27: S231-40.

- <sup>25</sup>Maidment AD, Albert M, Thunberg S, Adelow L, Blom O, Egerstrom J, Eklund M, Francke T, Jordung U, Kristoffersson T, Lindman K, Lindqvist L, Marchal D, Olla H, Penton E, Rantanen J, Skolov S, Ullberg C, Weber N. (2005). Evaluation of a photon-counting breast tomosynthesis imaging system. Proc SPIE 5745.
- <sup>26</sup>Dobbins, JT. (2009). Tomosynthesis imaging: At a translational crossroads. Med Phys. 36(6): 1956-1967.
- <sup>27</sup>Kuo J, Ringer PA, Fallows SG, Bakic PR, Maidment ADA, Ng S. (2011). Dynamic Reconstruction and Rendering of 3D Tomosynthesis Images. Proceedings SPIE Medical Imaging 2011.
- <sup>28</sup>Acciavatti RJ, Mein SB, Maidment AD. (2012). Investigating Oblique Reconstructions with Super-Resolution in Digital Breast Tomosynthesis. Lecture Notes in Computer Science.7361:737-44.
- <sup>29</sup>Acciavatti RJ, Maidment AD. (2012). Observation of super-resolution in digital breast tomosynthesis. Med Phys. 39(12): 7518-39.
- <sup>30</sup>Lu Y, Chan HP, Wei J, Hadjiiski L, Samala R. (2013). Study of Image Quality in Digital Breast Tomosynthesis by Subpixel Reconstruction. Medical Imaging.
- <sup>31</sup>R. J. Acciavatti and A. D. A. Maidment, "Investigating the potential for super-resolution in digital breast tomosynthesis," in SPIE Medical Imaging, edited by N. J. Pelc, E. Samei, and R. M. Nishikawa (SPIE, Lake Buena Vista, FL, 2011), pp.79615K-1 - 79615K-12.